Fundamental Defect Complexes and Nanostructuring of Silicon by Ion Beams

by

Lasse Vines

Submitted
in partial fulfillment of the requirements
for the degree of
Philosophiae Doctor

Department of Physics
Faculty of Mathematics and Natural Sciences
University of Oslo

Series of dissertations submitted to the
Faculty of Mathematics and Natural Sciences, University of Oslo
Nr. 703

ISSN 1501-7710

Cover: Inger Sandved Anfinsen.
Printed in Norway: AiT e-dit AS, Oslo, 2008.

Produced in co-operation with Unipub AS.
The thesis is produced by Unipub AS merely in connection with the
thesis defence. Kindly direct all inquiries regarding the thesis to the copyright
holder or the unit which grants the doctorate.

Unipub AS is owned by
The University Foundation for Student Life (SiO)

To my grandfather

Abstract

Silicon technology has become a cornerstone for the technological advances in our society for the last five decades. For carrying on with minimization of electronic devices a huge effort has been directed toward the technological development and fundamental understanding of physical processes associated with the ion implantation into silicon. Indeed, in ion implantation the impurities are intentionally introduced into a matrix lattice with the help of accelerated ion beams selectively modifying the properties of the implanted area. In addition to the introduction of the doping impurity the penetrating ions create defects that can be electrically active potentially affecting the device performance. In spite of a long research activity in the field there are still several open fundamental questions remaining, and this thesis contributes to the understanding of ion implantation induced defect complexes in silicon.

Firstly, we have studied the electrical properties of vacancy type point defect complexes generated in single collision cascades during heavy ion bombardment of silicon. Because of a high generation rate of defects within the "ion track" regions, a characteristic pattern of nanochannels having modified Fermi levels due to the local compensation around each ion trajectory is formed in n-type Si. The phenomenon has been studied using spectroscopic and imaging techniques, specifically deep level transient spectroscopy (DLTS) and scanning capacitance microscopy (SCM). The SCM measurements show a characteristic random pattern of reduced SCM signal correlated with the density of the ion impacts. Moreover, a strong correlation is detected between the probing frequency and the emission rate of the single negative acceptor level of the divacancy ($V_2(-/0)$) in Si. Further, DLTS reveals a significant filling time increase for all electronic levels originated from vacancy complexes with increasing ion mass as probed within the ion track regions. The results of isochronal annealing studies of vacancy complexes generated by heavy ion implants are also explained in terms of the revisited local compensation model. An improvement of the model is proposed, where the divacancy is considered to be available in two fractions; (1) highly localized

centers along the core track regions (V_2^{dense}) and (2) centers located outside ion tracks (V_2^{dilute}). The relative abundance of V_2^{dense}/V_2^{dilute} is ion mass dependent. In this model the V_2^{dense} fraction does not contribute to the doubly negative divacancy ($V_2(=/-)$) signal due to local carrier compensation, and the DLTS amplitude of $V_2(=/-)$ is determined only by the V_2^{dilute} fraction. Our finding clarifies a long lasting discussion in literature on the DLTS amplitude difference between $V_2(-/0)$ and $V_2(=/-)$ in ion implanted n-type Si.

Secondly, the thesis contains an investigation of the dominant electron trap in p-type Si ($E_c - 0.25eV$), where E_c is the conduction band edge. The $E_c - 0.25eV$ trap has previously been ascribed to the boron interstitial-oxygen interstitial (B_iO_i) complex, but our study shows no oxygen and only a weak boron dependence on the intensity of the level, challenging the B_iO_i identification.

Finally, the thesis explores the use of defect engineering by introducing nano-sized vacancy clusters (cavities) when synthesizing buried SiO_2 by ion implantation (SIMOX). Scanning spreading resistance microscopy measurements show that oxide nucleation can be enhanced by introducing cavities, potentially reducing the required oxygen dose during the SIMOX processing.

Acknowledgments

This thesis is the solid evidence of three years of research training in the physical electronics group at the University of Oslo. A period which have been motivating, frustrating, educating, interesting, exhausting, stressful and exciting. Just as the athlete depends on a good coach and a supporting team, the graduate student rely on good advisers, supportive colleagues, friends and family in order to develop the necessary research skills. I would therefore like to express my gratitude to my supervisors; my main supervisor Andrej Yu. Kuznetsov for introducing me to this topic, and for his enthusiasm for my work during the last three years, and my co-supervisors Bengt. G. Svensson for his skillful and experienced supervision giving me the confidence in the completion of this thesis, and Edouard V. Monakhov for his day to day supervision and hands-on guidance, and for acting as Wikidepia on semiconductors when conventional search methods failed.

I have also had the privilege to collaborate with Jens Jensen at Uppsala University, who have conducted the impressively low dose implantations reported in this thesis and added valuable contributions and inputs to my study, and Dr. Reinhard Kögler at Forschungzentrum Rossendorf, who introduced me to defect engineering of SIMOX processing and offered many inputs and interesting discussions. The in-house processing could not have been carried out without the assistance from our dedicated engineers in the MiNa lab, Viktor Bobal and Thomas Marthinsen. Thank you all!

I would also like to thank my colleagues at the MiNa lab; my "room mates" Klaus M. Johansen and Mads Mikelsen, and the rest of the group for all the relevant and irrelevant discussions, and for making my three years as a PhD student as interesting and joyful as they have been.

Finally, I would like the thank my wife, Birgitte, for supporting me and challenging me throughout my pregraduate, graduate and the coming postgraduate period, and for making it all worthwhile.

Contents

List of included papers

I **Visualization of MeV ion impacts in Si using scanning capacitance microscopy**
L. Vines, E. Monakhov,B. G. Svensson, J. Jensen, A. Hallén, and A. Yu. Kuznetsov
Phys. Rev. B **73**, 085312 (2006)

II **Scanning probe microscopy of Single Au ion implants in Si**
L. Vines, E. Monakhov, K. Maknys, B. G. Svensson, J. Jensen, A. Hallén and A. Yu. Kuznetsov
Materials Science & Engineering C, **26**, 782 (2006)

III **Ion mass effect and annealing behavior of vacancy complexes in swift ion implanted Si**
L. Vines, E. Monakhov, B. G. Svensson, J. Jensen and A. Yu. Kuznetsov
Submitted to Phys. Rev. B

IV **On the origin of the dominating electron trap in irradiated p-type silicon**
L. Vines, E. Monakhov, A. Yu. Kuznetsov, R. Kozłowski, P. Kaminski and B. G. Svensson
Submitted to Phys. Rev. B

V **Scanning spreading resistance microscopy of defect engineered low dose SIMOX samples**
L. Vines, R. Kögler and A. Yu. Kuznetsov
Microelectronic Engineering, **84**, 547 (2007)

Related publication but not included in the thesis

I **Study of defect engineering in the initial stage of SIMOX processing** R. Kögler, A. Mücklich, L. Vines, D. Krecar, A. Kuznetsov and W. Skorupa *Nucl. Intrum. Methods Phys. Res. B*, **257**, 161 (2007)

Chapter 1

Introduction

When an energetic heavy ion penetrates a solid target, it is slowed down by interaction with the target electrons and the target nuclei. The interaction between the energetic ion and a target nucleus can be treated as a screened Coulomb scattering event, that is an elastic collision between a moving ion and an atom at rest. The interaction results in an energy transfer from the ion to the lattice atom. In crystals, if the energy transfer is high enough, the atom can leave its lattice site and a Frenkel pair, an atom at an interstitial site and a vacancy, is generated. After the generation, both interstitials and vacancies can migrate, which can result in their annihilation or formation of stable defect complexes and larger extended defects (e.g. dislocation loop, cavities, etc.). The incident ion interacts also with both valence and core electrons of the target. Due to the high mass ratio between ions and electrons and the large number of interactions, a continuum approximation, where the ion is considered to move in a viscous fluid, is usually applied.

Single crystalline silicon is a well known material, and is well suited for studying the processes associated with the damage induced by heavy ions. Moreover, the methods of ion implantation doping and synthesis are widely used in the electronic industry further motivating the understanding of fundamentals of defect clustering reactions in Si. For sufficiently low dose implantations, single collision cascades prevail in Si,

and implantation/irradiation of both electrons and heavy ions result in point defect generation, rather than formation of extended defects. The "simplest" case of the electron irradiation has been conveniently used for studying point defects in Si for several decades due to the generation of a quite uniform distribution of vacancies and self-interstitials (Frenkel pairs). For heavy ion implantation the generation of Frenkel pairs is significantly stronger, resulting in a non-uniform defect profile around the ion trajectory. It has been a longstanding discussion in the literature of how far the implantation induced vacancies migrate before they form stable defect complexes within and around the ion trajectory. In spite of considerable advances in theoretical approaches, it is still difficult to perform reliable simulations of the defect reactions induced by ion implantation since the time scale of the events spans from $\sim 10^{-12}$ s to several minutes or days at room temperature. From an experimental point of view no direct imaging of the electrically active defect distribution around an ion trajectory in Si has been reported so far since the corresponding defect concentrations are below the detection limit of conventional microscopy techniques motivating the introduction of new techniques (Papers I and II). In addition, novel imaging techniques providing not only structural but also functional (e.g. electrical) characterization of the samples are interesting to apply when studying initial stages of ion implantation synthesis.

In addition to imaging techniques, there are also several spectroscopic methods applicable to study point defects and defect clusters in Si. In this thesis the deep level transient spectroscopy (DLTS) was employed, which is a well established technique for investigation of electrically active defects in semiconductors. The studies are focused on DLTS signatures of two charge states of a divacancy (two nearby vacancies forming a stable configuration [1], V_2) . Since the two charge states arise from the same defect, the intensity of the DLTS signal for these states are expected to be the same. While the one-to-one correlation holds for V_2 formed by electron irradiation or light-ion implantation, a deviation from the one-to-one correlation is observed for V_2 formed by heavy ion implantation. Several models have been proposed explaining the deviation. One model,

which has been explored in this thesis (Paper I-III), proposes that the local density of the defects (specifically divacancies) within an ion track region is high enough to cause local compensation and pinning of the Fermi-level to the deeper charge state of V_2, suppressing the filling of the shallower V_2 state and reducing its DLTS intensity (Paper III). This idea is interesting both for the fundamental understanding of the ion induced damage in Si and for potential applications. Indeed, providing the local carrier concentration around the ion trajectories is significantly altered compared to that in the bulk, nanosized channels with a reduced carrier density are formed, consistent with the interpretation of images in Paper I and II.

During the work on this thesis, several related findings and issues have occurred. For example, while studying the divacancy in p-type Si, the behavior of the dominating electron trap in boron doped material showed a boron dependence not previously reported, suggesting that our understanding of interstitial related defects is incomplete. This observation and its interpretation is pursued in Sec. 4.2 and Paper IV. Moreover, addressing the reactions resulting in extended defects the role of larger vacancy clusters formed after the ion implantation was investigated. Specifically the influence of cavities on the initial stages of ion implantation SiO_2 synthesis was studied. This topic is introduced and explored in Sec. 4.3 and Paper V.

The thesis is organized as follows: Chapter 2 introduces the basic equations for understanding semiconductors and point defects in semiconductors, hereby forming the basis for understanding Technology CAD simulations, which are presented at the end of the chapter. Chapter 3 describes the experimental techniques used in this work, while Chapter 4 highlights the work presented in the following papers.

Chapter 2

Basics of charge carriers and point defects in semiconductors

This chapter presents the fundamental equations used in semiconductor physics, and aims to serve as a basis for understanding the simulations carried out in the attached papers, and the experimental methods used in this thesis.

2.1 Basics of charge carriers in semiconductors

2.1.1 The Poisson and continuity equations

The Poisson equation is a part of Maxwells equations and relates the change in electrostatic potential, $\nabla\Psi$, to the charge density. For a semiconductor it can be defined as [2] [3]

$$\nabla \cdot \epsilon \nabla \Psi = -q \left(p - n + N_d - N_a \right), \tag{2.1}$$

where ϵ is the permittivity of the semiconductor, p is the hole density, n is the electron density, N_d is the density of ionized donors, N_a is the density of ionized acceptors, and q is the elementary charge. The Poisson equation, together with the continuity equations for electrons and holes, accounts for the transport of electrons and holes in and out of

a region and for the generation or recombination of electron-hole pairs. They form a powerful framework for understanding a variety of phenomena observed in solid state electronics. The continuity equations [3] for electrons and holes are,

$$\nabla \cdot \overrightarrow{J}_n = \quad qR + q\frac{\partial n}{\partial t}, \tag{2.2}$$

$$-\nabla \cdot \overrightarrow{J}_p = \quad qR + q\frac{\partial p}{\partial t}, \tag{2.3}$$

where $\overrightarrow{J}_n$ and $\overrightarrow{J}_p$ are the current densities for electrons and holes, respectively, and R is the net electron-hole recombination rate. The Poisson equation and the transport equations will constitute a set of differential equations to be solved. However, to successfully solve these equations additional models are needed, that describe for example, the electron-hole recombination R and the current densities.

2.1.2 The drift-diffusion approximation

Assuming that drift and diffusion of charge carriers are the main mechanisms for charge transport, the so-called drift-diffusion approximation for the current densities of electrons and holes can be described as [3]:

$$\overrightarrow{J}_n = \quad qn\mu_n\mathcal{E} + qD_n\frac{dn}{dx}, \tag{2.4}$$

$$\overrightarrow{J}_p = \quad qp\mu_p\mathcal{E} - qD_p\frac{dp}{dx}, \tag{2.5}$$

where μ_n and μ_p are the electron and hole mobilities, respectively, D_n and D_p are the diffusion coefficient of electrons and holes, respectively, and $\mathcal{E}$ is the electric field.

The mobility describes how easily an electron or a hole moves in the semiconductor when subjected to an electric field. In an intrinsic semiconductor the mobility is limited by phonon scattering, which only depends on the temperature. In doped semiconductors the scattering can also occur due to the carrier interaction with the ionized impurities. Additionally, in high electric fields the carrier scattering related to the field effect can become significant and must also be taken into consideration. In

the present work, only the phonon scattering [4] and a model (the Masetti model [5]) for the impurity (dopant) scattering have been used.

The effective intrinsic density of e.g. electrons is related to the band gap of the semiconductor, and can be calculated from $n_{i,eff} = n_i \exp \frac{\Delta E_g}{2k_B T}$ [6] [7] if both doping dependence and band gap narrowing are included, where n_i is the intrinsic density for an undoped semiconductor and given by $n_i = \sqrt{N_C(T) N_V(T)} \exp -\frac{E_g}{2k_B T}$. Here, E_g is the band gap, k_B is Boltzmanns constant, T is the absolute temperature, ΔE_g includes the band gap narrowing effect, N_C is the effective conduction band density of states, and N_V is the effective valence band density of states.

At room temperature, one can consider p- and n-type dopants in Si fully ionized. Thus $N_d^+ = N_d$ and $N_a^- = N_a$ for extrinsic semiconductors, and can be readily inserted into Eq. 2.1. However, at reduced temperature some of the dopant atoms will not be ionized, lowering the carrier concentration. The concentration of ionized donors, N_d^+ will be reduced with temperature according to [6] $N_d^+ = \frac{N_d}{1+g_D \exp \frac{E_F - E_D}{k_B T}}$, where g_D is the degeneracy factor and follows from the Fermi-Dirac distribution, E_D is the donor activation energy, and E_F is the Fermi level.

2.1.3 The Fermi-level

The Fermi level (or Fermi energy) is related to the fact that electrons obey Fermi-Dirac statistics, and represents an important quantity in semiconductor physics. The Fermi-Dirac distribution function gives the probability that an available energy state will be occupied by an electron, $f(E) = \frac{1}{1+\exp(E-E_F)/k_B T}$. Hence, an energy state at the Fermi level has the probability of 1/2 of being occupied by an electron [3]. However, in an ideal semiconductor there are no available states within the band gap, and therefore no possibility of finding an electron there. Hence, the available states are found in the tail of the distribution. The Fermi level for an intrinsic semiconductor is located close to the middle of the bandgap, while for instance in a n-type semiconductor the Fermi level is pushed towards the conduction band. Assuming that the Fermi level

lies at least several k_BT below the conduction band, one can approximate the carrier concentration of e.g an n-type semiconductor as $n = N_c \exp -(E_c - E_F)/k_BT$, where E_c is the conduction band edge and N_c is the effective density of states in the conduction band. In non-equilibrium situations, when the carriers are injected or generated, it is not meaningful to use the Fermi level, thus quasi Fermi levels for electrons and holes are frequently introduced instead.

2.1.4 pn-junction

When semiconductors of different conductivity are put together an equilibrium solution would require that the Fermi level in the materials is constant. For example in a *pn*-junction, carriers near the interface will diffuse over to the other side creating a space charge region depleted of free charge carriers, or a depletion region if an abrupt transition is assumed (the depletion approximation), in order to satisfy Eq. 2.1. Thus, requiring charge neutrality, an expression for the width of the depletion region, W, in a one dimensional structure can be stated as [3]

$$W = \sqrt{\frac{2\epsilon(V_0 - V)}{q}\frac{N_a + N_d}{N_d N_a}} \tag{2.6}$$

where V_0 is the built in voltage and V is the applied voltage. A similar expression can be found for a Schottky barrier, i.e. a rectifying semiconductor-metal contact. The junction and its depletion region can be considered as a parallel plate capacitor, and this concept is of uttermost importance both in semiconductor devices and in our case in probing point defects in the band gap by e.g. deep level transient spectroscopy (DLTS, see Sec. 3.1). The resulting capacitance, C, becomes

$$C = \frac{\epsilon A}{W} \tag{2.7}$$

where A is the contact area.

2.2 Point defects in semiconductors

2.2.1 Formation of defects

In our case of low dose ion implantation, the elastic collision between the energetic ion and a host atom can result in vacancy (V) and interstitial (I) generation (Frenkel pair) if the energy transfer is above a threshold value. Depending on the amount of energy transfered between the initial ion and the lattice atom (the interstitial), the interstitial can accelerate and collide with other lattice atoms, creating a collision cascade. The collision cascades are more pronounced for heavier ions compared to lighter ions and electron irradiation. In a collision cascade, two nearby vacancies can for example form a divacancy (two nearby vacancies forming a stable configuration V_2 [1]), which is stable at room temperature. Such defect generation are spatially correlated, and thus confined within the ion trajectory.

The primary defects, the vacancies and interstitials, are highly mobile at room temperature, and will migrate around in the lattice, potentially forming defect complexes with other defects or annihilate by e.g. a vacancy interstitial recombination or at sinks (e.g. a surface). In fact, only a few percentage of the generated vacancies and interstitials escape mutual recombination [8]. From the surviving V and I, a complex hierarchy of competing reaction involving both interstitials and vacancies will evolve, resulting in secondary defects. By secondary defects one usually refers to all irradiation induced defects that are thermally stable at room temperature. The amount and identity of the irradiation induced defects depend on the material and type of irradiation, in particular on the type and concentration of impurities.

During thermal treatments, a defect can either migrate or dissociate, resulting in annealing of certain defects and formation of others. Thus, by careful examination of the thermal evolution of a defect, insight about the nature (e.g. the kinetics) of a defect can be obtained.

2.2.2 Electrical properties of defects

Defects can have a significant influence on the properties of a semiconductor. A defect, either extended (one to three dimensional structures) or not (zero dimensional structure or point defect), alter the periodic potential of a crystal, which leads to formation of additional electronic states. Defects can be defined as electrically active or inactive. Electrically active defects form states in the forbidden band gap, which can donate or accept electrons to/from the conduction band (E_C) or valence band (E_V). If the state is neutral when it is filled by an electron, and positive if the state is empty, it is defined as a donor, while if the state is neutral when it is empty and negative when it is filled by an electron, the state is called an acceptor. The donor or acceptor level can occur close to the conduction or valence band edge, respectively, and is then called a shallow state. States located further away from the band edges are usually called deep levels, and can act as generation or recombination centers. It is primarily the shallow levels that are used for doping of semiconductors. However, their electrical impact on a device structure can be mainly handled through the equations in the previous section, and are not the prime target here.

2.2.3 Shockley-Read-Hall statistics

Consider a point defect having a state in the band gap with an energy E_T below the conduction band. According to Shockley, Read [9] and Hall [10] this state can capture or emit an electron or hole from the conduction or valence band, respectively. Fig. 2.1 shows the charge interaction between the defect and the conduction and valence band. Trapping of electrons from the conduction band and holes from the valence band occur at rates of nc_n and pc_p, respectively, where c_n is the electron capture coefficient and c_p is the hole capture coefficient. The capture coefficient can be defined as

$$c_{n(p)} = \sigma_{n(p)} \nu_{th,n(p)}, \tag{2.8}$$

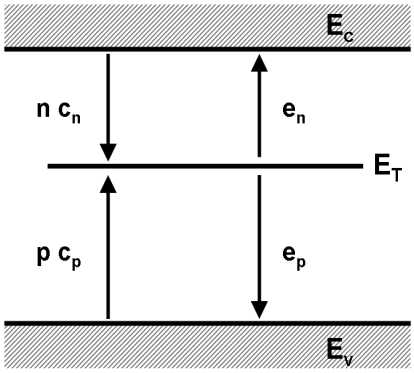

Figure 2.1: Schematics of the charge carrier processes to and from a defect level, showing the capture (nc_n) and emission (e_n) of electrons from the conduction band (E_c), and capture (pc_p) and emission (e_p) of holes from the valence band (E_v).

where $\sigma_{n(p)}$ is the capture cross section of an electron or a hole and $\nu_{th,n(p)} = \sqrt{\frac{3k_BT}{m^*_{n(p)}}}$ is the electron (hole) thermal velocity, and $m^*_{n(p)}$ is the effective electron (hole) mass. Further, the trap can emit electrons and holes to the conduction or valence band, respectively, and this process occurs at a rate of e_n and e_p. The probability for a filled electron trap to emit its electron to the conduction band is given by [9] [11]

$$e_n = \nu_{th,n}\frac{g_0}{g_1}\sigma_n N_C \exp -\frac{\Delta G}{k_BT} \tag{2.9}$$

$$= \nu_{th,n}\frac{g_0}{g_1}\exp\frac{\Delta S}{k_B}\sigma_n N_C \exp -\frac{\Delta H}{k_BT}, \tag{2.10}$$

where g_1 is the degeneracy of an occupied state, g_0 is the degeneracy factor of an unoccupied state, $\Delta G = \Delta H - T\Delta S$ is Gibbs free energy, ΔH is the enthalpy, and ΔS is the entropy. A similar expression can be made for the emission of a hole.

Depending on the values of the capture and emission coefficients, some of the processes shown in Fig. 2.1 will be dominating. For example, if the dominating process is trapping of electrons from the conduction band (nc_n) with the subsequent re-emission

to the conduction band (e_n) the center acts as a trap, while if the trapping of the electron is followed by a trapping of a hole from the valence band (pc_p), i.e. a recombination of an electron hole pair, the level acts as a recombination center.

The occupancy of a level f, for instance an acceptor level, can be expressed as [6]:

$$\frac{\partial f}{\partial t} = \sum_i r_i = \sum_i (1-f)c_i - fe_i, \tag{2.11}$$

where r_i is the net capture rate, and i denotes the process involved, e.g. the capture and emission of an electron from the conduction band. For $f = 1$ the level is fully occupied, while for $f = 0$ the level is completely empty. For example, in a stationary state ($\frac{\partial f}{\partial t} = 0$), and neglecting electron capture from the valence band and hole capture from the conduction band, the occupancy becomes $f = \frac{c_n + c_p}{c_n + e_n + c_p + e_p}$.

2.3 Device simulation using Technology Computer Aided Design (TCAD)

The electrical behavior of a semiconductor structure or device can be modeled and simulated using the basic physical models stated in Sec. 2.1 and 2.2, where the Poisson and the transport equations are the governing equations. The geometrical structure can be modeled by dividing the structure into small elements, or grid, having a specific set of properties given by the equations in the previous sections, and interacting with neighboring elements. Hence, the electrical characteristics of the simulated device is described by a set of partial differential equations, which can be numerically solved by for example an iterative approach, i.e. guessing on a solution or assuming a set of starting condition and repeating the calculations until the solution has converged with an acceptable small predefined error. The parameters being solved are the quasi Fermi potentials, while other parameters such as electron densities are being recomputed from the solution.

Several commercial software programs exist utilizing the physical and transport equations as described above. In the work carried out in this thesis the device simulator of Synopsys Technology CAD (TCAD) has been used. The development of TCAD simulations started out in the late 1960's to assist the growing bipolar technology, and is still closely related to the IC industry. However, the basic principles of TCAD make it a powerful tool for investigating and understanding fundamental semiconductor properties and measurement results, for example the electrical behavior of a defect level with a concentration having a non-uniform spatial distribution (Paper III).

Chapter 3

Experimental techniques

In this chapter, three methods for electrical characterization are presented. Deep level transient spectroscopy (DLTS) is a macroscopic technique widely used in point defect characterization, while both scanning spreading resistance microscopy (SSRM) and scanning capacitance microscopy (SCM) are techniques for the nanometer scale, mapping resistance and capacitance in two dimensions, respectively.

3.1 Deep level transient spectroscopy

Point defects are important from an application point of view due to their influence on the electric current and capacitance performance of a device. On the other hand, this performance modification can be utilized to study and extract fundamental information about the crystal abnormalities and their electrical characteristics. For example, by measuring the current or capacitance characteristics of a *pn*-diode or a Schottky contact, the charge capture and emission properties, including activation energies, of a point defect can be extracted.

In a depletion region of a pn-junction the free charge carriers are swept out by the electric field arising between the two regions, as discussed in Sec. 2.1, resulting in a region, W (Eq. 2.6), totally depleted of free charge carriers. Deep level transient

spectroscopy (DLTS) [12] is an experimental technique utilizing the depletion region capacitance modification in temperature and time domains as a function of applied voltage providing information about electronic trap levels.

3.1.1 Principle of operation

In DLTS the applied bias voltage is alternately fixed between a smaller (filling pulse) and a larger voltage (reverse bias). Consider a deep acceptor type electron trap of concentration N_t, where $N_t \ll n$, close to a Schottky barrier in n-type Si. During the filling pulse the steady state depletion width $W(0)$ is small, where the defect levels outside $W(0)$ is below the Fermi level and will therefore trap charge (Fig. 3.1). After a sudden increase in reverse bias the depletion region increases to $W^*(V)$, and the traps between $W(0)$ and $W^*(V)$ are arisen above the Fermi level (Fig. 3.1). At this moment, the occupied traps start to release the electrons to the conduction band at a rate given by Eq. 2.9. Due to the electric field the electrons will be swept away with a negligible amount of re-trapping, and the depletion region will decrease, because of charge re-distribution, to the steady state region, $W(V)$ (Fig. 3.1). λ is the width of the region with partial filling of the trap level during the filling state of the measurement, Fig. 3.1, and given by $\lambda = \sqrt{\frac{2\epsilon(E_F - E_T)}{qN_d}}$. The same arguments can also be made for pn-junctions and donors and hole traps in p-type Si. Thus, the re-emission of carriers can be detected by the influence on the junction capacitance through a transient detection technique.

The measurements are carried out while scanning the appropriate temperature range, changing the emission rate of the defect levels in accordance with Eq. 2.9, and recording the capacitance transients by adjusting the temperature so that the emission rate corresponds to a predefined time window, one has a mean to separate the energy levels from each other in the form of characteristic peaks or signatures, as illustrated in Fig. 3.2.

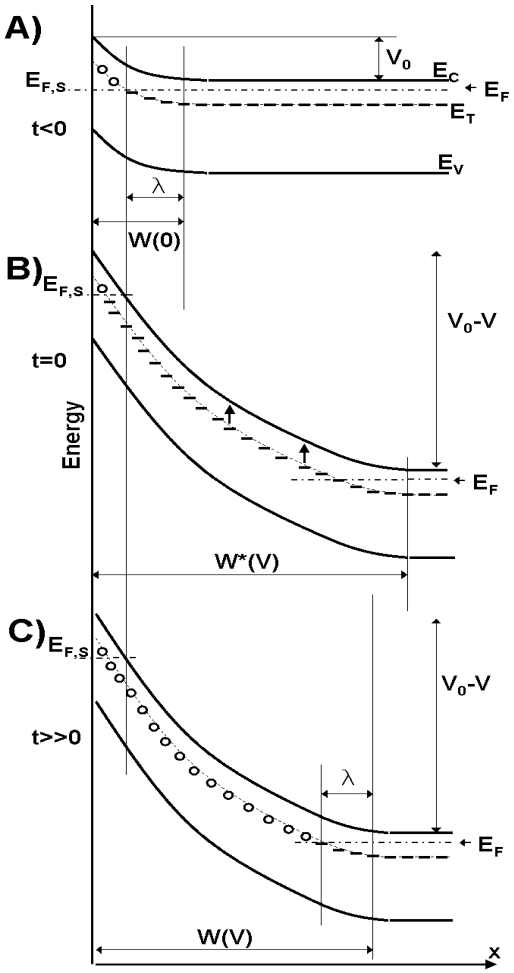

Figure 3.1: An illustration of the band bending in n-type Si versus the distance from a Schottky barrier metallurgical contact (a) during the filling pulse ($t < 0$), (b) immediately after the increase in reverse bias ($t = 0$), and (c) after emission of the trapped carriers, in the steady state reverse bias regime ($t \gg 0$). $W(0)$, $W^*(V)$ and. $W(V)$ represents the depletion region at $t < 0$, $t = 0$ and $t >> 0$ respectively, while the built-in voltage and reverse bias are labeled as V_0 and V, respectively, λ is a transition region partially occupied by electrons, $E_F, E_{F,S}$ is the Fermi level of the bulk and Schottky contact, respectively.

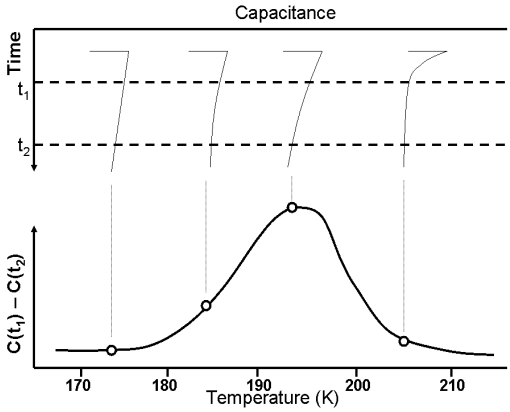

Figure 3.2: Schematics of the construction of a DLTS spectrum from the difference in junction capacitance transients between two fixed times t_1 and t_2 at different temperatures.

3.1.2 Obtaining electrical characteristics

3.1.2.1 Trap concentration

The change in capacitance, $C(t_1)-C(t_2)$, is found by constructing a DLTS signal by applying a weighting function to the capacitance transient. The change is proportional to the trap density, and for the temperature where the DLTS signal from a defect level peaks, the change in capacitance can be shown to be (applying Eqs. 2.1, 2.7 and 2.6 for the situations in Fig. 3.1)

$$\left[\frac{\Delta C}{C}\right]_x = -\frac{n(x)}{N_d W^2} x \Delta x. \tag{3.1}$$

If the amount of point defects are small so that $\Delta C \ll C$, that is $W^*(V)-W(V) \ll W(V)$ in Fig. 3.1, the capacitance signal becomes a simple exponential decay and the amplitude is directly proportional to the trap density. Furthermore, if the trap density is uniformly distributed in the measurement region, an integration of Eq. 3.1 from $W(0)-\lambda$ to $W(V)-\lambda$ results in

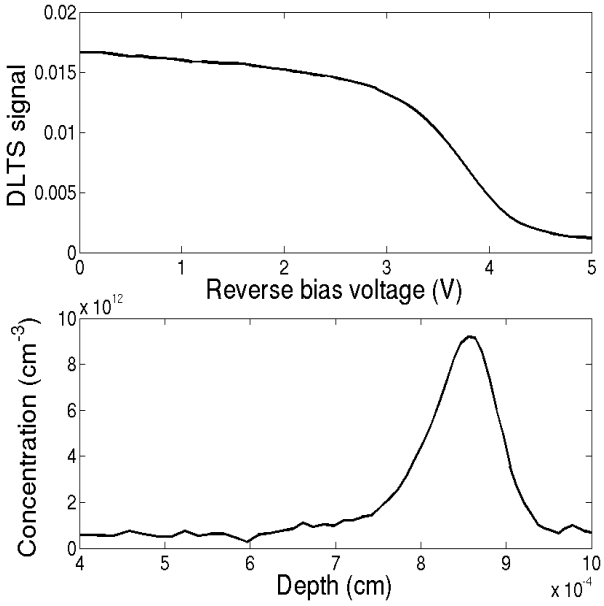

Figure 3.3: (a) DLTS intensity as a function of reverse bias voltage during filling and (b) the corresponding defect concentration profile versus depth.

$$\frac{\Delta C}{C} = -\frac{N_t}{2N_d}\left[1 - 2\frac{\lambda}{W(V)}\left(1 - \frac{C(V)}{C(0)}\right) - \left(\frac{C(V)}{C(0)}\right)^2\right], \tag{3.2}$$

relating the change in capacitance to the trap concentration. An often appropriate assumption is neglecting the edge regions, that is by setting $\lambda = 0$ and $C(0) \gg C(V)$, where the relation between change in capacitance and trap density can be expressed as $N_t = \frac{2\Delta C}{C} N_d$ [12]. However, in some cases the bracketed terms in Eq. 3.2 can become substantial.

3.1.2.2 Depth profiling

For nonuniform defect profiles, for instance in samples subjected to heavy ion implantations, the trap density relation in Eq. 3.2 does not hold. To obtain the number

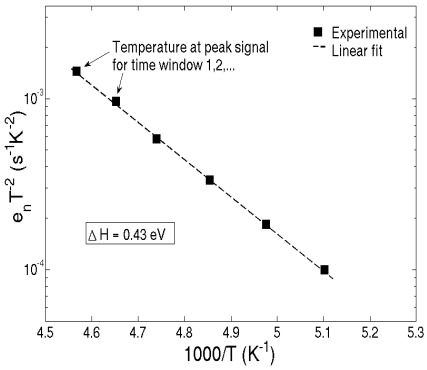

Figure 3.4: Arrhenius plot of ion implanted n-type Si made from a DLTS spectra with time windows in the range 20-640 ms.

of defects in the measurement region one must integrate over the defect profile, that is one must obtain a depth profile of the trap levels. One approach for depth profiling of a level is to systematically increase the probing volume by increasing the applied voltage during the filling pulse (Fig. 3.3(a)), keeping the steady-state reverse bias voltage constant. A specific trap level is studied by keeping the temperature at the maximum response of the trap (Fig. 3.3). Assuming an asymmetric junction or a Schottky barrier, and that $\Delta C \ll C$, an incremental change in the relative capacitance due to a small change in the pulse voltage, a depth profile is found to be [12]

$$\frac{d\left(\Delta C/C\right)}{dV} = \left(\frac{\epsilon}{qW^2 N_d}\right) \frac{N_t(x)}{N_d(x)}. \tag{3.3}$$

3.1.2.3 Activation energy

The activation energy of a level can be extracted from an Arrhenius plot of the measured temperature at the peak maximum for different time windows of the transient detection (e.g. changing t_1 and t_2 in Fig. 3.2). The slope and intercept at $1/T = 0$ is related to the activation energies and capture cross sections through Eq. 2.9 (Fig.

3.4). Rewriting Eq. 2.9 to the form $\ln(e_n/T^2) = \ln(\sigma_\infty Q) - \Delta H/k_B T$, where Q is a constant factor, one can readily obtain the activation energy (ΔH) from the slope in the Arrhenius plot and the effective capture cross section (σ_∞) from the extrapolated offset of this line at $1/T = 0$. However, a more accurate and direct method for measuring the capture cross section, or in general studying the filling of a defect level, is by measuring the filling time of a trap level. The filling time can be measured by increasing the duration of the filling pulse while monitoring the DLTS signal keeping the temperature constant at the DLTS peak maximum for the given defect level. For example, during the filling of an electron trap (in n-type) the amount of trapped charge will in a first approximation be $N_T f = N_T[1 - \exp(-c_n t)]$, where the capture cross section can be extracted from the capture coefficient according to Eq. 2.8.

3.1.3 Minority carrier transient spectroscopy (MCTS)

DLTS is used to obtain information about electrically active majority carrier traps, but information about minority carrier traps can also be extracted. If a net forward bias of a *pn*-junction is allowed during the filling pulse, minority carriers are injected and can get trapped, and remitted again during the transient capacitance capture period. This version of DLTS is called minority carrier transient spectroscopy (MCTS). Minority carriers can also be generated optically (ODLTS) [11]. In MCTS, the injection of carriers will not be limited by the doping concentration, but by the barrier height, and by the diffusion length of the minority carriers. In addition, since a forward bias is used during the filling pulse, the near surface region (Fig. 3.1) will also be filled and contribute to the overall trap concentration. Both majority and minority carriers are present in the sample during the filling pulse. Hence the minority carrier trapping level must have a significantly larger minority capture cross section than majority carrier capture cross section. Otherwise an electron-hole recombination will dominate over re-emission and the trap level will be "unsaturable", and therefore difficult to observe in the MCTS spectrum.

3.2 Electrical characterization using scanning probe microscopy

Scanning probe microscopy (SPM) is a family of related techniques based on the scanning of a sharp probe tip over a sample surface while measuring material properties such as topography, electrical and/or magnetic characteristics. SPM originates from the development of the scanning tunneling microscope by Binning and Rohrer in 1981 [13] and later the atomic force microscope by Binning, Quate and Gerber in 1986 [14]. In STM the tunneling of electrons between a tip and a sample is utilized in keeping a constant separation while scanning the tip, in which a two-dimensional profile of the surface topography at the atomic scale is extracted. The technique requires a conductive sample surface, in addition to very stable measuring conditions, and is therefore usually operated in ultra high vacuum conditions (UHV). The strict sample requirements motivated the development of the atomic force microscope (AFM). In AFM a sharp tip at the end of a cantilever is scanned across the sample surface and the interaction force between the tip and the sample is found by measuring the cantilever deflection, as illustrated in Fig. 3.5. A sharp tip is required, typically with a radius of 2-40nm, and the system can measure both conducting and insulating samples and is more robust than STM towards environmental disturbances.

The AFM can be operated in several modes, called i) contact mode, where the tip is in mechanical contact with the sample while scanning, ii) tapping mode, where the tip is oscillating and thus "tapping" the sample surface, and iii) non-contact mode, where the tip is scanned in proximity of the sample measuring the attractive force between tip and sample.

After the invention of the STM and AFM, which basically measure the topography of a sample, a series of related techniques have been tested measuring electrical, mechanical and magnetic properties, and are commonly called SPM as stated above. The scanning capacitance microscopy (SCM) [15] [16] and scanning spreading resistance

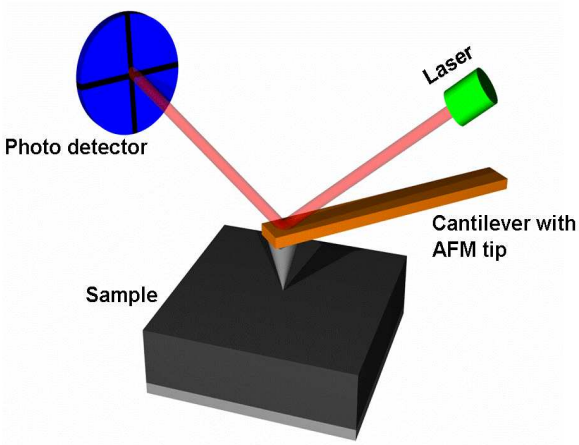

Figure 3.5: Schematics of the AFM principle, where a tip at the end of a cantilever is scanned over the sample surface. The cantilever deflection, and thus the surface topography, is monitored using the reflection from a leaser beam.

microscopy (SSRM) [17] are particularly interesting in measuring/imaging electrical properties of semiconductors.

3.2.1 Scanning spreading resistance microscopy

3.2.1.1 Principle of operation

Scanning spreading resistance microscopy is an SPM method operating in contact mode, maintaining a constant force between the tip and the sample, and measuring the local spreading resistance in the sample simultaneously with its topography. To extract the spreading resistance an electrical circuit is made up of a conductive probe tip, the sample and a read out unit including a current amplifier, as shown in Fig. 3.6. Normally a logarithmic current amplifier is applied measuring currents from about $10\,pA$ to $0.1\,mA$, corresponding to a carrier concentrations typically between 10^{14} and $10^{20}\,cm^{-3}$.

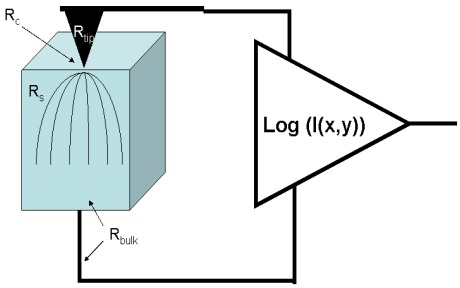

Figure 3.6: Illustration of the electrical circuit utilized in SSRM measurements, indicating different resistance contributions

For a conductive AFM tip in direct contact with a semiconductor the resistance, R_{tot}, of the system is given by:

$$R_{tot} = R_s + R_c + R_{tip} + R_{bulk}, \tag{3.4}$$

where R_s is the spreading resistance, R_c is the contact resistance, R_{tip} is the resistance of the probe tip, and R_{bulk} includes the bulk resistance, the back contact resistance and the resistance in the readout unit.

The spreading resistance is related to the resistivity ρ of the material, and hence the carrier concentration through the equations

$$R_s = \frac{\rho}{A_{tip}}, \tag{3.5}$$

$$\frac{1}{\rho} = \sigma = qn\mu_n + qp\mu_p, \tag{3.6}$$

$$\tag{3.7}$$

assuming an ideal ohmic contact, where ρ is the resistivity of the sample and A_{tip} is the effective contact size, and σ is the conductivity. For a cylindrical contact $A_{tip} = 4 \times r_{cyl}$ [18], where R_{cyl} is the radius of the cylinder, while $A_{tip} = 2\pi \times r_{hem}$ [18] for a probe tip shaped as a hemisphere with radius r_{hem}. Since the radius of the tip is small, typically $10 - 40\,nm$, R_s is large and can dominate the total resistance if the other contributions in Eq. 3.4 are kept sufficiently low. Hence, in a well designed experiment the SSRM resistance is inversely proportional to the carrier concentration. Moreover, Eq. 3.7 can be used as a first order approximation to quantify the carrier concentration.

To obtain a low contact resistance, R_c, a large force between the tip and sample is applied, typically in the range of $1 - 50\,\mu N$, penetrating any oxide layer and plastically deforming the Si region underneath [19]. The tip will therefore scratch the sample making repeating scans in the same region difficult. To have a low probe resistance, R_{tip}, the conductivity of the probe tip must be high. In addition, the probe tip should ideally be sharp to give a high lateral resolution, hard enough to withstand the high pressures between tip and sample, and preferably very resistant to wear and tear. Typical probes used in SSRM are etched Si tips coated with doped diamond or metal (e.g. an inner layer of Ti and an outer layer of Pt), where the doped diamond tips are preferred in studies of Si samples. However, the probe resistance of the doped diamond tips can influence measurements on low resistivity samples [19]. The bulk resistance term in Eq. 3.4, R_{bulk}, includes both the bulk resistivity of the sample, the contact resistance of the back contact and the resistivity of the readout unit, and must also be kept sufficiently low.

Additional complications of the conversion of SSRM resistance into sample resistivity or carrier concentrations arise since a scanning nanosized electrical contact is rarely ohmic, and the measured resistance will therefore depend on the applied bias requiring the recording of a structure at several bias voltages. Secondly, the contact size is difficult to determine, both because the tip size changes between tips and after tip wear, and because the effective electrical contact size can differ from the geometrical

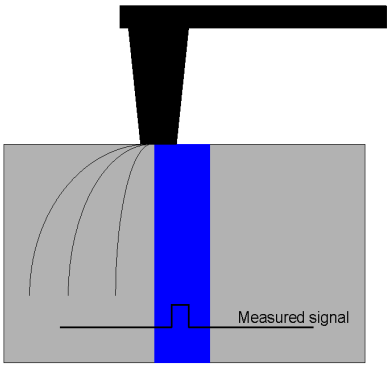

Figure 3.7: Schematics of spreading resistance measurements across a buried oxide layer, showing a reduced width of the oxide signature of the SSRM resistance.

size. Thirdly, surface charges may influence the resistance measurement in low doped samples, and both surface charges and probe resistance will influence the linearity of the resistance response. Finally, measuring close to edges, grain boundaries, interfaces, or in samples with large resistivity gradients, the changing resistivity profile will influence the spreading resistance, as illustrated in the example of measuring a buried oxide layer in Fig. 3.7.

3.2.1.2 Quantification

To quantify the measured resistance response a preferable method is therefore to convert the SSRM resistance into resistivity or carrier concentration through calibration [19], either of the test structure itself (e.g. using additional measurements such as 4 point probe), or preferably by specially prepared calibration structure(s). If the calibration structure involves several resistivities over the dynamic range of interest, the linearity of the resistance response can be addressed as well as the absolute resistivity. However, to convert the SSRM resistance into carrier concentrations, information about

the mobility is necessary (Eq. 3.7).

3.2.1.3 Sample preparation

The sample preparation procedures depend on the material and application. Plan view measurements are relatively straight forward, where an oxide removal and back side contact formation using a conductive glue are normally sufficient. For cross section measurements, standard procedures have been developed for Si [19], involving cleaving, mounting on support structure, polishing and back contact formation. However, for other materials, such as e.g. ZnO and InP, and in some Si studies a simple cleaving and backside contact formation can be sufficient.

3.2.2 Scanning capacitance microscopy

Scanning capacitance microscopy (SCM) is operated in contact mode, but in contrast to SSRM, it measures the changes in capacitance instead of resistance.

3.2.2.1 Principle of operation

The measurements rely on a metal-insulator-semiconductor (MIS) structure, as illustrated in Fig. 3.8 where the conductive tip represents the metal, and an oxide usually represents the insulator. Hence, the tip operated in SCM mode does not penetrate the oxide layer. In an ideal one dimensional system, the total capacitance C_{tot} of the MIS/MOS structure is the series combination of the oxide capacitance C_{ox} and the semiconductor capacitance C_s

$$\frac{1}{C_{tot}} = \frac{1}{C_{ox}} + \frac{1}{C_s}. \tag{3.8}$$

In the depletion approximation, the oxide and the semiconductor can be characterized using a parallel plate capacitor, as described in Sec. 2.1, that is $C_{ox} = \frac{\epsilon_{ox} A_{tip}}{d_{ox}}$ and

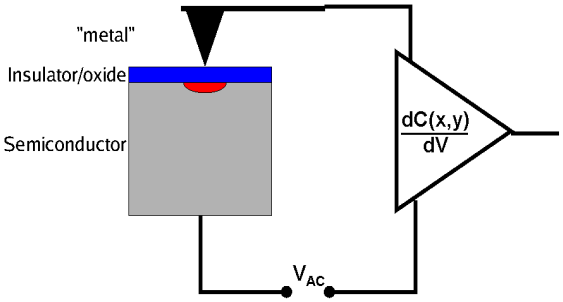

Figure 3.8: The electrical circuit of an SCM measurement, where the blue layer illustrates the oxide layer, and the red region illustrates the space charge region formed by the tip sample interaction.

$C_s = \frac{\epsilon_s A_{tip}}{\sqrt{\frac{2\epsilon_s(V_0-V)}{qN_d}}}$, where ϵ_{ox} and ϵ_s are the permittivity of the oxide and semiconductor, respectively, and d_{ox} is the oxide thickness. Thus, the total capacitance can be written

$$C_{tot} = \frac{A}{\left(\sqrt{\frac{2(V_0-V)}{\epsilon_s q N_d}} + \frac{d_{ox}}{\epsilon_{ox}}\right)}. \tag{3.9}$$

However, due to the small contact size, the total capacitance of the MOS structure is small. For example, a Pt tip with contact radius of 40 nm, and a Si sample with a doping concentration of $N_d = 10^{17}\ cm^{-3}$ and a 3 nm oxide, the total capacitance becomes $3 \times 10^{-18}\ F$, which is lower than any stray capacitance in the measuring circuit. Thus, in order to record the signal from the tip- sample system, the change in capacitance, $\frac{dC}{dV}$, is utilized instead. The derivative of Eq. 3.9 is inversely proportional to the carrier concentration, $dC/dV \propto N_d^{\alpha}$, where α is a negative number. In other words, the SCM signal (or $\frac{dC}{dV}$) of a moderately doped sample is larger than the signal

from a highly doped sample. Moreover, as seen from Eq. 3.9, the SCM signal is independent of the mobility, in contrast to other measuring techniques such as SSRM.

To elaborate on the properties of the SCM (dC/dV) signal, let us consider the typical capacitance-voltage (CV) curve for a moderately doped p-channel (n-substrate) MOS structure as shown by the (lower) blue curve in Fig. 3.9. Applying an alternating voltage using a moderate frequency ($\sim 50 - 100\,kHz$) and with an amplitude ΔV superimposed on a dc voltage, the MOS structure is alternating between weak accumulation and depletion. The resulting change in capacitance is measured, ΔC (see Fig. 3.9), using an ultra high frequency ($\sim 1GHz$) capacitance meter [20]. To maximize the output signal the dc bias voltage is operated around the flat band voltage. Hence, for a low and moderately doped semiconductor the amplitude of ΔC is large compared to a highly doped material, Fig. 3.9.

Further, the phase of the measured ΔC compared to ΔV can be used to distinguish p-type and n-type material, due to the polarity change in the MOS structure, as illustrated by the blue and red ΔC line in Fig. 3.9. Hence, a 180° phase shift is observed between n and p-type material.

In the discussion above a MOS structure has been assumed. However, SCM measurements can also be carried out on samples without an oxide layer if a Schottky barrier with sufficient quality is established between the tip and the sample.

3.2.2.2 Resolution

The resolution in SCM is related to the probing volume formed by the space charge region underneath the tip [21] (see the red region in Fig. 3.8). The fundamental limitation is given by the screening length of the charge carriers, the Debye length [22], given by $L_D = \sqrt{\frac{\epsilon_s k_B T}{q^2 n}}$. However, a practical length scale limitation is given by the width of the depletion region (see Eq. 2.6). Naturally, the resolution depends on the applied bias and the carrier concentration. For example, Si with doping concentration $10^{18}\,cm^{-3}$ the screening length and the depletion width would be about 4 and 20 nm,

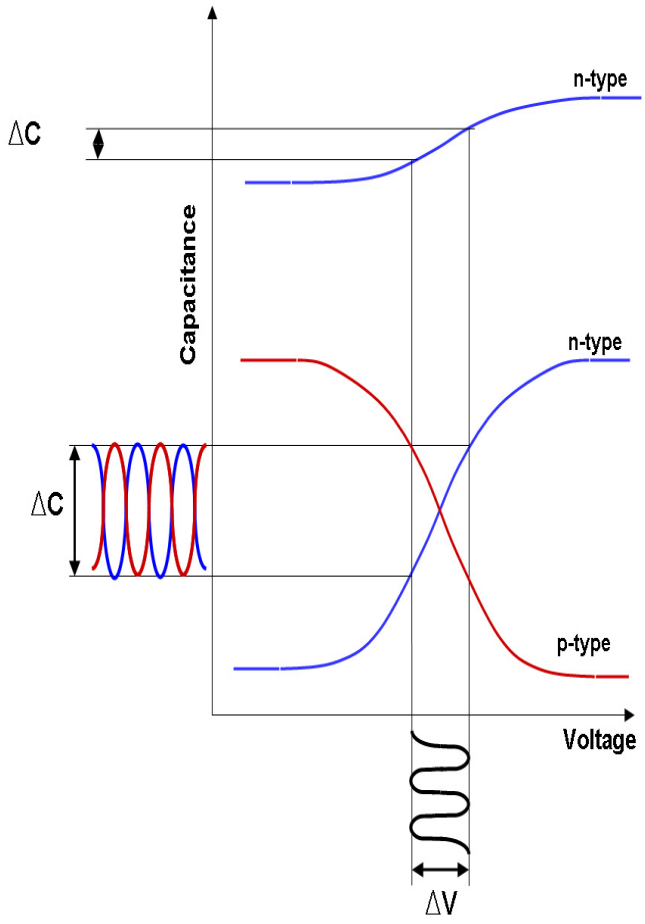

Figure 3.9: Schematics of typical CV curves from n and p-type Si. The introduction of an alternating voltage results in a alternating capacitance with an amplitude ΔC and a phase. The blue capacitance curves illustrates a moderately (lower) and highly (upper) doped n-type material, while the red curve illustrates a moderately doped p-type material. The polarity of the material produces a phase difference in the two ΔC curves.

respectively, while in low doped samples, e.g. $N_d = 10^{15}\ cm^{-3}$, the corresponding numbers would be ~ 130 and $670\,nm$. However, taking the tip radius and shape into account, the lateral resolution can be considered as a convolution between the tip size and the depletion region. Thus, in materials with a high doping concentration the tip radius can significantly influence the lateral resolution, while in low doped materials the resolution, both laterally and in depth, would be given by the depletion region.

3.2.2.3 Tip characteristics and sample preparation

The main difference between the tips used in SSRM and SCM is the force constant of the cantilever on which the tip is mounted. In SCM this force constant is approximately one order of magnitude lower, reducing the applied force between the tip and the sample, and hence, not penetrating the oxide layer. Thus, both the surface roughness and oxide are important in obtaining good quality measurements. Procedures for sample preparation have therefore been developed [20], where a routine procedure for cross section measurements include stacking, sawing, gluing and polishing steps, in addition to low temperature oxidation to control the thermal oxide. Similar procedures can be carried out for plan view measurements as well. However, depending on the initial wafer quality and amount of processing steps applied to the structure, some steps can be omitted.

3.2.2.4 Towards quantitative SCM

A non-linear expression relating the carrier concentration and the dC/dV amplitude of the SCM signal can be found from the one dimensional expression in Eq. 3.9. However, a SCM measurement is three dimensional in nature, complicating the simple expression in Eq. 3.9. Moreover, the three dimensional tip shape must be included for a proper evaluation of the resulting SCM signal, in addition to the uncertainties in uniformity and size of the oxide layer. Thus, traditionally SCM has been used as qualitative tool, and this is also the case for the work reported in this thesis. However,

efforts have been made developing SCM into a quantitative tool [16]. In the recent years encouraging results have been obtained for well controlled test samples using a calibration curve method [23], where the calibration curves are developed using reference samples and SCM simulation software. It is also worthwhile to mention that observations of spatial feature sizes down to $1nm$ have been reported [22]. Anyhow, the most crucial reason for using SCM in the present thesis is the ability to record local charge influencing the depletion region capacitance.

Chapter 4

Point defects and ion induced nanostructuring in Si

This chapter aims to provide a short description of the studies that have been performed and highlight the main results obtained. The first section is devoted to the fundamental study of local compensation after heavy ion impacts in n-type Si. The second section focus on the nature of the dominating electron trap observed in p-type Si, while the third section is devoted to the investigation of the role of large vacancy clusters and cavities on the initial stages of ion implantation synthesis of SiO_2.

4.1 Point defect structures after heavy ion implantation

4.1.1 Motivation

There is a longstanding discussion in the literature of how far the irradiation/implantation induced vacancies can migrate at room temperature in Si before they form stable defect complexes, e.g. the divacancy V_2. In ion irradiated samples, the vacancies are formed within a narrow region around the ion trajectory, as estimated by TRIM [24]. The

divacancy can form both by direct interaction when two consecutive Si atoms are displaced by the impinging ion [1], and by pairing of two migrating monovacancies [25]. V_2 is one of the most fundamental, and one of the most disputed, defect complexes occurring after electron and ion irradiation, having two negative charge states in the band gap. Its doubly negative charge state, $V_2(= /-)$, was identified due to its 1:1 correlation with the singly negative charge state ($V_2(-/0)$) after electron irradiation [26]. However, a deviation from this 1:1 correlation was observed, when bombarding with protons and α-particles [27], and heavier ions [28]. Several models were introduced to explain this deviation, including (i) strain in the heavy ion collision cascades preventing the motional averaging of the V_2 state favoring $V_2(-/0)$ over $V_2(= /-)$ [28] [8] [29], (ii) additional levels e.g. larger vacancy clusters (V_x, $x > 2$) contributing to the DLTS intensity at $E_c - 0.42eV$ [30], and (iii) local carrier compensation due to high divacancy concentration ($[V_2]$) around the ion trajectory so that much less electrons are available to fill the doubly negative state [31] [32] [33]. For the latter model, the local compensation model, the observed DLTS behavior has been linked to the migration length of irradiation generated vacancies [32].

To motivate the idea of the local compensation, assume a 600keV Si impact in Si, creating a maximum of 7 vacancies/ion/nm, as found by averaging over 400 impacts using TRIM simulations (using a displacement energy of $15\,eV$). Presuming only 1% [8] of the generated vacancies form V_2, and that the migration length is less than $15nm$ (Paper III), the peak V_2 concentration becomes $\sim 10^{17}\,cm^{-3}$, which is higher than most of the doping concentrations used in DLTS studies. For a higher concentration of deep acceptors than shallow donors, a depletion of carriers is expected, pinning the Fermi-level at the deep acceptor state, and developing an energy barrier around the disordered region, as illustrated in Fig. 4.1(a). Thus, the barrier will lower the amount of electrons available for occupying states closer to the conduction band, such as $V_2(= /-)$. However, this pinning will be local, and the surrounding matrix will modify the local compensation by supplying additional charge, as seen in Fig. 4.1(b) for the

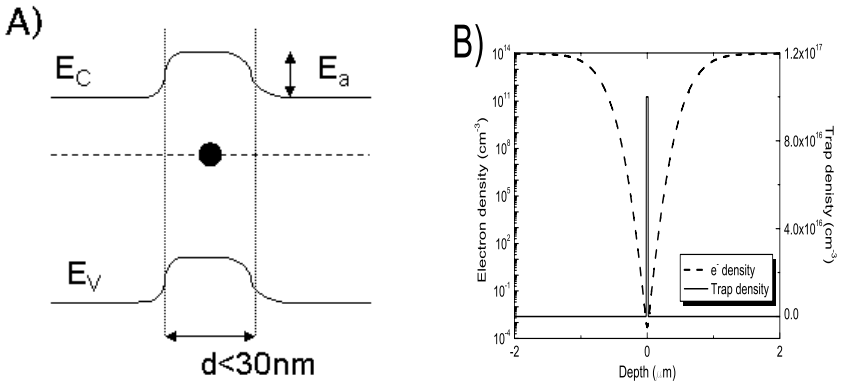

Figure 4.1: (a) Schematics of the band bending around the disordered region in n-type Si having a sufficiently high density of electron traps to pin the Fermi level to the defect level, where E_C and E_V are the conduction and valence band edge, respectively, and E_a is the barrier developed by the Fermi-level pinning. (b) Simulation of the electron (dashed line) density for n-type Si using Cartesian coordinates and with doping concentration of $1 \times 10^{14}\, cm^{-3}$ and a trap concentration of $2 \times 10^{17}\, cm^{-3}$ formed within a radius of $15nm$(solid line).

defect channel estimated above, and with a bulk doping concentration of $1 \times 10^{14} cm^{-3}$. The distribution of the space charge region around the ion trajectory will depend on both the defect concentration and the bulk doping concentration. In the example at hand, Fig. 4.1(b), the radius of the space charge region is on the order of $\sim 500nm$.

4.1.2 Visualization

The discussion of defect production from ion impacts are mainly based on DLTS studies. DLTS is a macroscopic measurement technique [12], where the capacitance transients over a large (typically $> 1 \times 10^{-2}\, cm^2$) area are recorded. To verify a local compensation effect, i.e. the fact that the defect distribution after heavy ion impacts are highly nonuniform and can significantly alter the local charge concentration, a microscopic technique would be beneficial. With the advances in atomic force microscopy (AFM), in particular with the development of scanning spreading resistance microscopy (SSRM) and scanning capacitance microscopy (SCM), such opportunities become available. SCM measures the change in local capacitance in the near surface region of a sample, see Sec. 3.2.2, and can be utilized for visualizing the local distribution of charge concentration.

Fig. 4.2 shows an SCM image of a 3 MeV Au impact in Si, where a random pattern of reduced dC/dV values with diameter between 150 and 600 nm is observed. The pattern is interpreted as increased charge concentration within the probing volume due to the introduction of electrically active point defects after the ion impact. The pattern is not correlated to the topography of the measurement region and not observed in a non-implanted reference sample. Furthermore, by varying the temperature of the sample a reduction in SCM contrast is observed between 35 and $50°C$. In this temperature range the probing frequency of the SCM system, being operated at $50 - 100\, kHz$, coincides with the emission frequency of the single charge state of the divacancy strongly indicating that the local charge distribution is caused by ion induced point defects, that is V_2, in the bulk Si (Paper I).

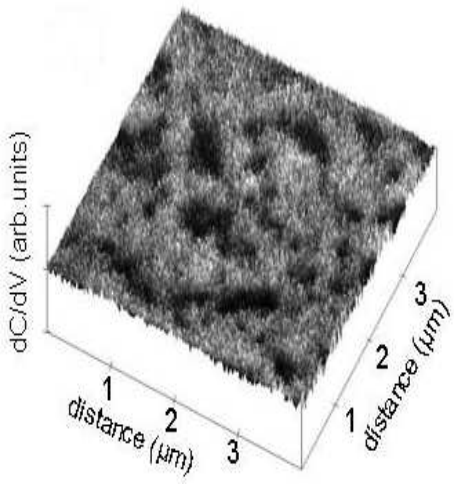

Figure 4.2: SCM image of a 3 MeV Au impact in n-type Si (doping $1 \times 10^{16}\, cm^{-3}$).

The SCM results also show a distinct dose dependence, where the number of features are significantly lower than the number of ion impacts. For example, from 3 MeV Au impacts in Si no features are observed for impact doses lower than $2 \times 10^{8}\, cm^{-2}$, while a dose of $8 \times 10^{8}\, cm^{-2}$ showed approximately 20 features, and a dose of $5 \times 10^{9}\, cm^{-2}$ showed 60 features. However, the probing volume is, as discussed in Sec. 3.2.2, related to the screening length, or the depletion region. Thus, the SCM measurements will show the convolution between a relatively large probing volume and the defect size. Several models can explain this non-linear dose dependence, for example the amount of induced defects in the near-surface regions varies resulting in only a fraction of tracks visible by SCM, or several nearby tracks are necessary to exceed the upper noise level of the system (Paper II).

An alternative macroscopic technique for showing the local compensation effect could have been to probe $V_2(-/0)$ and $V_2(= /-)$ in p-type material by MCTS (see Sec. 3.1), since here the carrier concentration would mainly be limited by the barrier

height of the *pn*-junction and not the doping concentration, thus potentially result in a complete occupancy of $V_2(=/-)$, restoring the 1:1 correlation between the two charge states. However, both $V_2(-/0)$ and $V_2(=/-)$ have a large hole capture cross section, promoting recombination of carriers rather than re-emission to the conduction band. Thus, $V_2(-/0)$ and $V_2(=/-)$ cannot be observed by MCTS in p-type samples.

4.1.3 Simulation and annealing behavior

To improve our understanding of the effect of local compensation, a simulation model was developed and explored. The model was developed within the drift-diffusion transport approximation using the commercially available Synopsys software [34]. A circular symmetry has been applied, and defect levels resembling the divacancy ones were introduced in a narrow, but adjustable, region around the center of the structure. The simulations show that by using the average defect generation, as found by TRIM [24], an incomplete occupancy occur for heavy ions, but not for light ions, in moderately and low doped structures. This indicates that a model based on the average vacancy generation is incomplete.

It is known that the defect production from a single ion impact is highly nonuniform, having defect rich regions around the secondary cascades surrounded by defect lean Si matrix. Therefore, a refined version of the model proposed in Ref. [32] is introduced. In this model the divacancies are decomposed into two fractions. First fraction is V_2's located in high density defect regions (V_2^{dense}), having a concentration of $V_2(-/0)$ sufficient for reducing the occupancy of $V_2(=/-)$. Second fraction of V_2 is located in regions with lower density of defects (V_2^{dilute}), where a complete occupancy of all defect levels occur (Paper III). This modified local compensation model shows good agreement with the ion mass effect on $V_2(=/-)$ observed by DLTS.

To evaluate the modified local compensation model, and to gain more information about the annealing properties, an annealing study of ion implanted Si was carried out using high-purity epitaxial layers, in contrast to previously reported annealing studies

on ion implanted float zone (Fz) or Czochralski (Cz) Si [35]. In impurity lean Si, divacancy migration is promoted over hydrogen passivation ($V_2 + 2H \rightarrow V_2H_2$) [36] at temperatures above $\sim 200°C$, and can be verified by the transition $V_2 + O \rightarrow V_2O$ as a shift in the peak temperatures [37][38].

Chemical Vapor Deposited epitaxial Si samples, having a bulk doping concentration in the epitaxial layer of $1 \times 10^{14}\, cm^{-3}$, were irradiated by He, C, Si and I with energies from 2.75 to 48 MeV, and with doses between 5×10^6 and $3.5 \times 10^8\, cm^{-2}$. Isochronal heat treatments were carried out in $25°C$ steps of 20 min duration. The results show a decreasing intensity of $V_2(-/0)$ after $\sim 200°C$, although $V_2(= /-)$ stays constant, or even increases, until it anneals out at around $325°C$. An increase in the VO amplitude is also observed, and the increase of both $V_2(= /-)$ and VO is more pronounced with increasing ion mass. Filling pulse measurements of the samples showed a reduced filling with ion mass, but an increased filling with annealing temperature.

The annealing properties of V_2 is consistent with the two mode divacancy model. Indeed, V_2^{dense} the average distance between V_2 is small, where the migration length of only a few nm can be sufficient for divacancies to meet and form larger defect clusters, reducing the overall $V_2^{cluster}$ concentration and the local band bending around the secondary cascades. In addition, the V_2 migration will increase the characteristic width of V_2^{dense}, further reducing the Fermi level pinning. The reverse annealing effect, in addition to the reduced filling of both $V_2(= /-)$ and VO is a strong argument in favor of the local compensation model.

4.2 On the origin of the dominating electron trap in p-type Si

The acceptor states of the divacancy cannot be observed by MCTS in p-type Si due to their large hole capture cross sections [39]. Interestingly, a dominant defect level, hereafter called E1, is observed by MCTS around $V_2(= /-)$, and was first observed

by Kimerling [40]. In addition to V_2 and E1, the most prominent point defects in p-type Si are VO [41] [42], the carbon interstitial C_i [43], and carbon-interstitial-oxygen-interstitial C_iO_i [44]. Mooney et al. proposed an identification of E1, having a level position of $E_c - 0.25\,eV$, as B_iO_i [45]. A reduced MCTS signal was observed for samples with a reduced boron concentration, and this dependence was the main argument for proposing the B_iO_i pair. In later publications by Kimerling, Drevinsky and coworkers [46] [47], additional studies on E1 was carried out supporting the boron dependence and therefore strengthening the B_iO_i identification. Another argument for the identification was a correlation between the annealing of B_i and the rise of the E1 level, as observed by Harris [48]. In later years, theoretical studies supported the B_iO_i identification [49] by claiming that the defect would have a donor like state around $E_c - 0.24\,eV$. However, different groups found different stable configurations of this defect [50] [51], suggesting that the center was not fully understood. All the reported data on the E1 level was carried out using Cz or Fz material, and samples with different processing treatments were simultaneously compared. Furthermore, the expected competition between C_s and the B_s as traps for the Si self-interstitial has not been fully explored. Additional data on the E1 level is, therefore, desirable, and Paper IV is such a contribution.

Mesa structured n^+pp^+ diodes were fabricated from epitaxially grown Si with boron doping concentrations in the range $6 \times 10^{13} - 2 \times 10^{15}\,cm^{-3}$ and Cz grown samples with doping concentration of $1.5 \times 10^{15}\,cm^{-3}$. The diodes were irradiated either by 6 MeV electrons or 1.8 MeV protons to different doses. The measured MCTS spectra showed that the level was observed, and even dominating, at B concentration lower than previously reported, Fig. 4.3, and the generation rate was slightly decreasing with increasing B concentration, contradicting the earlier reported $[B_s]$ dependence [47] ($[B_s]$ denotes concentration of substitutional boron).

Boron interstitials become mobile above $\sim 240\,K$ [48], and the proposed reaction mechanism for generating the B_iO_i complex involves two reactions: $I + B_s \rightarrow B_i$ and

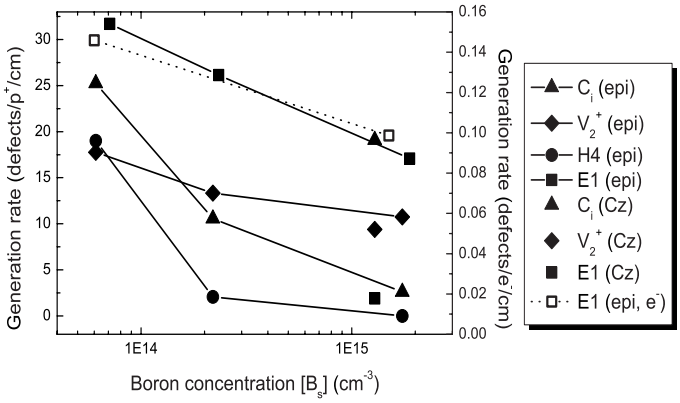

Figure 4.3: Generation rate of the dominating point defects as a function of doping concentration for epitaxial (symbols + lines) and Cz (symbols) as measured immediately after proton irradiation. In addition, open symbols connected by a dashed line represents the results measured for the E1 level after electron irradiation in epitaxial material.

$B_i + O_i \rightarrow B_iO_i$, where I generated by the irradiation kicks out a boron substitutional, which migrates until it encounters an oxygen interstitial. Thus, the process can be limited by the concentrations of B_i and/or O_i. However, the measurements can not be explained by $[O_i]$ limiting the reaction, since oxygenated samples of the $2 \times 10^{15}\ cm^{-3}$ material did not give an increased E1 concentration. In addition, a one-to-one correlation between the loss of $[C_i]$ and growth of $[C_iO_i]$ is observed in all the samples, indicating an abundance of oxygen. Hence, the identification of E1 as B_iO_i is challenged.

Several possibilities exists to explain the $[B_s]$ dependence of E1. Firstly, in order to preserve the existing B_iO_i model, an unobservable defect level might influence the $[B_s]$ dependence of E1. In fact, in a recent paper by Yarykin et al. [52] it has been claimed that B_iC_s, which previously has been identified as having a level at $E_v + 0.29\,eV$, is electrically inactive, and will form at the expence of B_iO_i. Secondly, as previously reported for Cz materials, B_iB_s can limit the formation of B_iO_i. However, in Cz this occurs for $[B_s] \gtrsim 2 \times 10^{16}\ cm^{-3}$, but with low carbon concentrations this threshold value may decrease. Thirdly, an alternative identification for the E1 defect must be considered, where boron-carbon and boron-hydrogen related centers are some of the possible alternatives. One potential candidate in this respect is B_iC_i since it would have a complex formation characteristics. For a low C concentration, the generation of B_i would dominate, and the formation of B_iC_i is limited by C_i, in accordance with the present results. However, for large C concentrations compared to B, the generation of C_i will prevail over B_i, and the formation of B_iC_i is limited by B_s in accordance with Refs. [45], [46] and [47]. This is, however, very speculative and needs further confirmation.

4.3 Defect engineering of SIMOX structures

Formation of big vacancy clusters and even cavities can be promoted by high dose noble gas element implantation, e.g. He. It is known that a He implantation followed by a heat treatment causes firstly the formation of He bubbles. Secondly, He atoms diffuse out and leave behind an empty cavity with a typical size of a few nanometers [53] [54]. Such large vacancy clusters or cavities located inside the crystal can be efficient nucleation sites when synthesizing buried SiO_2 by ion implantation. The precipitation cites can be manipulated by for example adjusting the implantation energy.

One possible and interesting application of such precipitation, and which is explored in Paper V, is in defect engineering of buried oxide layers for SOI manufacturing through the SIMOX process (Separation by IMplanted OXygen) [55]. In the SIMOX process a buried oxide layer is formed by an oxygen implantation and subsequent heat treatment. The typical oxygen dose is large, and hence costly, and is one of the reasons why the competing "Smartcut^{TM}" process [56] has become the leading technology for SOI production today. However, if one can reduce the oxygen dose necessary for forming a complete oxide layer, SIMOX will be an interesting and competitive alternative. To reduce the necessary oxygen dose a smaller width of the buried oxide layer must be achieved, which is now given by the straggling of the O implantation profile. Creating precipitation sites for oxygen growth within a narrow depth region in the initial stage of the buried oxide formation, one can potentially enhance the precipitation here and thus narrowing the thickness of the layer.

Furthermore, during SiO_2 precipitation, Si self interstitials are known to be released [57] and one additional measure to facilitate the SiO_2 precipitates is to create extra sinks for self interstitials, for example by dislocation loops outside of the SiO_2 reaction zone. Thus, for example a dual O and Si implantation can both supply the reaction with oxygen, and form gettering sites for the excess interstitials.

The main functional parameter of a buried oxide (BOX) layer is its resistivity, and

Sample	Mean SiO_2 precipitation band width (nm)	Mean grain size (nm^2)	Total oxide area within scan ($1 \times 1\,\mu m$) (nm^2)
Oref	89.7	1120	7.39×10^3
He + O	56.4	1790	1.00×10^4
O + Si	94.2	1420	8.70×10^3
He + (O +Si)	89.5	1270	6.58×10^3

Table 4.1: List of grain statistics obtained by the nanoscope software for the different samples

can be measured either macroscopically by monitoring the current through a BOX layer, or microscopically by SSRM (see Sec. 3.2.1). SSRM is applied to cross-sections of the BOX samples for measuring the thickness of a BOX layer, or the oxide grains if a complete oxide is not yet formed. The technique offers the advantages of being a relatively fast method avoiding complicated sample preparation, and it provides a measure of the oxygen contributing to an increase in the local resistivity.

In order to explore the defect engineering of SIMOX structures, and to evaluate the applicability of using SSRM for such studies, three different defect engineered samples were produced and compared with a reference sample (without defect engineering, Oref). The defect engineered sample consisted of a part containing the nanocavities (He+O), a part with end of range defects produced during the oxygen implantation by a dual Si and O implantation (O+Si), and a part both containing nanocavities and end-of-range defects (He + (O+Si)). The end-of-range defects were produced by a 1.1 MeV Si^+, having a larger projected range than the 200 keV O implants, so that the end-of-range defects were produced outside the reaction zone. The O and Si doses were 6×10^{16} and and $1 \times 10^{17}\,cm^{-2}$, respectively.

Multiple measurements were carried out for all samples, and used to extract grain statistics. An example of a SSRM measurement is shown in Fig. 4.4, and the grain

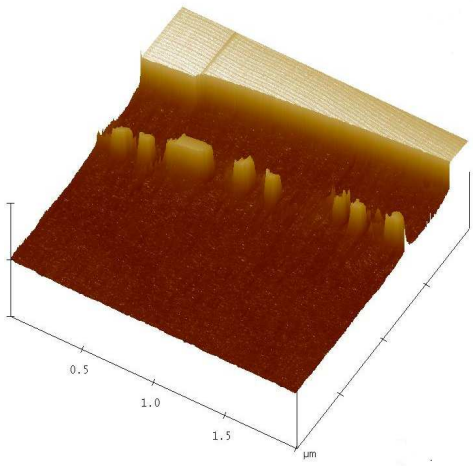

Figure 4.4: SSRM image of a defect engineered (He + O) sample showing the oxide grains. Increased SSRM values represent increased resistivity.

statistics are shown in Tab. 4.1. The results show that the area of the SiO_2 grains detected in the sample (He + O) is larger than that of the reference sample, indicating that the He-induced nanocavities facilitate nucleation and enhance SiO_2 formation. Moreover, the characteristic width of the precipitates is also lower for (He + O) compared to Oref. The dual implantation results in a slight increase in measured total oxide area, while the characteristic width is similar to that in the reference sample.

In conclusion, the SSRM measurements show evidence for increased precipitation by using nanocavities in the initial stages of the oxide precipitation, while the end-of-range defects did not improve the precipitation. However, the process needs to be optimized and further studies are required before final conclusions can be drawn.

Chapter 5

Concluding remarks and suggestions for future work

The major part of this thesis is devoted to the understanding of defect clustering in heavy ion implantated Si. Firstly, progress has been made towards visualization of the local compensation after heavy ion impacts using SPM. Secondly, the local compensation model has been refined, decomposing the divacancy formation in V_2^{dilute} and V_2^{dense} components, where Fermi-level pinning mainly occurs around the secondary collision cascades. The model explains the ion mass dependence, and the simulations are found to be in good qualitative agreement with the experimental results. Finally, the annealing characteristics of heavy ion impacts in Si can be consistently described using the two mode divacancy model. However, the defect production after heavy ion impacts is complex, and further studies are needed.

One aim with studying heavy ion impacts in impurity lean material was to monitor the V_2 migration, and thus the evolution of local compensation, through the V_2O formation. Unfortunately, a hidden level around $V_2O(-/0)$, which also is observed in electron irradiated Si, complicated the analysis, and this idea was not fully exploited in Paper III. However, if the hiden level can be characterized or removed, the V_2 migration can be fully explored. Also in Paper III, it is expected that large vacancy clusters form after

annealing at temperatures above $200°C$, and this effect requires further characterization. In this respect, positron annihilation spectroscopy after several of the annealing steps reported in Paper III would be very interesting, carried out after a heavy ion bombardment such as I or Au in order to obtain a high enough defect concentration and to maximize the average distance between each ion track. Another interesting experiment would be to investigate heavy ion impacts using electron holography, in an attempt to visualize the potential as illustrated in Fig. 4.1.

The work described in Paper I-III is devoted to the fundamental understanding of heavy ion impacts in Si forming the basis of more application oriented studies. The first step toward applications would be contact formation, and in fact, this can be realized through a self alignment process utilizing the increased etch rate in the oxide layer after heavy energetic ion impacts [58]. A preliminary study was made in this thesis and Fig. 5.1 shows a topographical image of a contact formed after a Au implantation followed by wet etching, thermal evaporation of gold and subsequent lift-off. However, this process needs to be optimized, and in particular the contact size must be more well controlled.

Regarding the dominant electron trap in irradiated p-type Si, Paper IV shows that further studies on interstitial related point defects are needed, since the commonly adopted identification of the $E_c - 0.25\,eV$ level as B_iO_i is challenged. To obtain further insight into the behavior of the $E_c - 0.25\,eV$ level in impurity lean Si, DLTS studies including samples with well controlled and adjustable carbon and boron concentrations should be undertaken. In-situ DLTS measurements of the B_i to $E_c - 0.25\,eV$ transformation and a possible correlation with C_i should also be pursued.

Paper V shows that defect engineering has a potential for improving existing Si processes, for example in the formation of buried oxide layers through the SIMOX process. By forming nanosized vacancy clusters oxide nucleation can be enhanced, potentially reducing the required oxygen dose during the SIMOX process. However, the width of the BOX layer, and thus the precipitation, is very sensitive to the position of

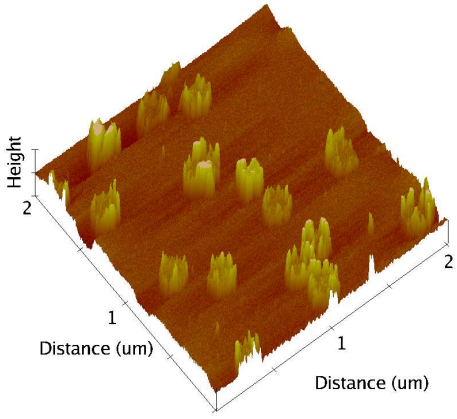

Figure 5.1: AFM image of the topography of a Si surface after Au implantation through a 200 nm oxide layer and subsequent wet etching and contact formation. The contacts are self-aligned over the ion tracks in the bulk Si.

the He induced nanocavities relative to that of the oxygen implantation profile. Hence optimization of the defect engineering process is necessary before final conclusions regarding the industrial applicability can be drawn.

Bibliography

[1] J.W. Corbett and G.D. Watkins *Phys. Rev. Lett.*, vol. 7, p. 314, 1961.

[2] S.M. Sze, *Physics of Semiconductor Devices*. John Wiley & Sons, 2nd ed., 1981.

[3] B.G. Streetman and S. Banerjee, *Solid State Electronic Devices*. Prentice Hall, 5th ed., 2000.

[4] C. Lombardi, S. Manzini, and A. Saporito *IEEE Transactions on computer-aided design of integrated circuits and systems*, vol. 7, no. 11, p. 1164, 1988.

[5] G. Masetti, M. Severi, and S. Solmi *IEEE Transactions on electron devices*, vol. 30, no. 7, p. 764, 1983.

[6] Synopsys, Inc., *Sentaurus Device*, x-2005.10 ed., 2005.

[7] S.A. Campbell, *The Science and Engineering of Microelectronic Fabrication*. Oxford University Press, 2001.

[8] B.G. Svensson, C. Jagadish, A. Hallén, and J. Lalita *Phys. Rev. B*, vol. 55, p. 10498, 1997.

[9] W. Shockley and W.T. Read *Phys. Rev.*, vol. 87, p. 835, 1952.

[10] R.N. Hall *Phys. Rev.*, vol. 87, p. 387, 1952.

[11] P. Blood and J.W. Orton, *The Electrical Characterization of Semiconductors: Majority Carriers and Electron States*. Academic Press, 1992.

[12] D.V. Lang *J. Appl. Phys.*, vol. 45, p. 3014, 1974.

[13] G. Binning, H. Rohrer, C. Gerber, and E. Weibel *Phys. Rev. Lett.*, no. 49, p. 57, 1982.

[14] G. Binnig, C.F. Quate, and C. Gerber *Phys. Rev. Lett.*, vol. 56, p. 930, 1986.

[15] C.C. Williams, J. Slinkman, W.P. Hough, and H.K. Wickramasinghe *Appl. Phys. Lett.*, vol. 55, no. 16, p. 1662, 1989.

[16] C.C. Williams *Annu. Rev. Mater. Sci.*, vol. 29, p. 471, 1999.

[17] P. D. J. Snauwaert, T. Clarysse, W. Vandervorst, and L. Hellemans *Appl. Phys. Lett.*, vol. 66, p. 1530, 1995.

[18] R. Holm, *Electrical Contacts, Theory and Applications*. Springer, 4th ed., 1967.

[19] P. Eyben, *Scanning spreading resistance microscopy: High resolution two-dimensional carrier profiling of semiconductor structures*. PhD thesis, Katholieke Universiteit Leuven, 2004.

[20] Veeco Application Module: Dimension and Multimode Manual, Software Version 5.12 r4, Rev D.

[21] J.J. Kopanski, J.F. Marchiando, and J.R. Lowney *J. Vac. Sci Technol. B*, vol. 14, p. 242, 1996.

[22] F. Giannazzo, V. Raineri, S. Mirabella, E. Bruno, G. Impellizzeri, and F. Priolo *Mat. Sci. Eng. B*, vol. 124, p. 54, 2005.

[23] F. Giannazzo, V. Raineri, S. Mirabella, G. Impellizzeri, F. Priolo, M. Fedele, and R. Mucciato *J. Vac. Sci. Technol. B*, vol. 24, no. 1, p. 370, 2006.

[24] J.F. Ziegler, J.P. Biersack, and U. Littmark, *The stopping and Range of Ions in Solids*. New York: Pergamon, 1985.

[25] B.G. Svensson and J.L. Lindström *J. Appl. Phys.*, vol. 72, p. 5616, 1992.

[26] A. O. Evwaraye and E. Sun *J. Appl. Phys.*, vol. 47, no. 9, p. 3776, 1976.

[27] A. Hallén, B.U.R. Sundquist, Z. Paska, B.G. Svensson, M. Rosling, and J. Tirén *J. Appl. Phys.*, vol. 67, p. 1266, 1990.

[28] B.G. Svensson, B. Mohadjeri, A. Hallén, J.H. Svensson, and J.W. Corbett *Phys. Rev. B*, vol. 43, p. 2292, 1991.

[29] R.M. Fleming, C.H. Seager, D.V. Lang, P.J. Cooper, E. Bielejec, and J.M.Campbell *J. Appl. Phys.*, vol. 102, p. 043711, 2007.

[30] N. Abdelgader and J.H. Evans-Freeman *J. Appl. Phys.*, vol. 93, p. 5118, 2003.

[31] N. Keskitalo, A. Hallén, J. Lalita, and B.G. Svensson *Mat. Res. Soc. Symp. Proc.*, vol. 469, p. 233, 1997.

[32] E.V. Monakhov, J. Wong-Leung, A.Yu. Kuznetsov, C. Jagadish, and B.G. Svensson *Phys. Rev. B*, vol. 65, p. 245201, 2002.

[33] L. Vines, E.V. Monakhov, B.G. Svensson, J. Jensen, A. Hallén, and A. Yu. Kuznetsov *Phys. Rev. B*, vol. 73, p. 085312, 2006.

[34] Synopsys Inc., 700 East Middlefield Road, Mountain View, CA 94043, USA; see also http://www.synopsys.com/.

[35] P. Pellegrino, P. Lévêque, J. Lalita, A. Hallén, C. Jagadish, and B.G. Svensson *Phys. Rev. B*, vol. 64, p. 195211, 2001.

[36] E.V. Monakhov, A. Ulyashin, G. Alfieri, A.Yu. Kuznetsov, B.S. Avset, and B.G. Svensson *Phys. Rev. B*, vol. 69, p. 153202, 2004.

[37] A. Kawasuso, M. Hasegawa, M. Suezawa, S. Yamaguchi, and K. Sumino *Appl. Surf. Sci.*, vol. 85, p. 280, 1995.

[38] M. Mikelsen, E.V. Monakhov, G. Alfieri, B.S. Avset, and B.G. Svensson *Phys. Rev. B*, vol. 72, p. 195207, 2005.

[39] A. Hallén, N. Keskitalo, F. Masszi, and V. Nágl *J. Appl. Phys.*, vol. 79, no. 8, p. 3906, 1996.

[40] L.C. Kimerling *IEEE Trans. Nucl. Sci.*, vol. 23, p. 1497, 1976.

[41] G. Bemski *J. Appl. Phys*, vol. 30, p. 1195, 1959.

[42] G.D. Watkins, J.W. Corbett, and R.M. Walker *J. Appl. Phys.*, vol. 30, p. 1198, 1959.

[43] A.R. Bean and R.C. Newman *Solid State Commun.*, vol. 8, p. 175, 1970.

[44] L.J. Cheng and P. Vajda *J. Appl. Phys.*, vol. 40, p. 4679, 1969.

[45] P.M. Mooney, L.J. Cheng, M. Süli, J.D. Gerson, and J.W. Corbett *Phys. Rev. B*, vol. 15, p. 3836, 1977.

[46] P.J. Drevinsky, C.E. Caefer, S.P. Tobin, J.C. Mikkelsen, and L.C. Kimerling *Mater. Res. Soc. Symp. Proc.*, vol. 104, p. 167, 1988.

[47] L.C. Kimerling, M.T. Asom, J.L. Benton, P.J. Drevinsky, and C.E. Caefer *Mater. Sci. Forum*, vol. 38-41, 1989.

[48] R.D. Harris, J.L. Newton, and G.D. Watkins *Phys. Rev. B*, vol. 36, p. 1094, 1987.

[49] J. Adey, R. Jones, and P.R. Briddon *Appl. Phys. Lett*, vol. 83, no. 4, p. 665, 2003.

[50] M. Sanati and S.K. Estreicher *Phys. Rev. B*, vol. 72, p. 165206, 2005.

[51] A. Carvalho, R. Jones, M. Sanati, S.K. Estreicher, J. Coutinho, and P.R. Briddon *Phys. Rev. B*, vol. 73, p. 245210, 2006.

[52] N. Yarykin, O.V. Feklisova, and J. Weber *Phys. Rev. B*, vol. 69, p. 045201, 2004.

[53] C.C. Griffioen, J.H. Evans, P.C. De Jong, and A. Van Veen *Nucl. Instrum. Methods. Phys. Res. B*, vol. 27, p. 417, 1987.

[54] W. Fukarek and J.R. Kaschny *J. Appl. Phys.*, vol. 86, p. 4160, 1999.

[55] R. Kögler, A. Mücklich, J.R. Kaschny, H. Reuther, F. Eichhorn, H. Hutter, and W. Skorupa *Solid State Phenom.*, vol. 108-109, p. 321, 2005.

[56] M. Bruel *Electronics Lett.*, vol. 31, no. 14, p. 1201, 1995.

[57] S.M. Hu *J. Appl. Phys.*, vol. 45, no. 4, p. 1567, 1974.

[58] J. Jensen, A. Razpet, M. Skupiński, and G. Possnert *Nucl. Instr. Methods Phys. Res. B*, vol. 245, no. 1, p. 269, 2006.